



ARL-RP-0580 • OCT 2016



Microstructural Effects on the Spall Properties of ECAE-Processed AZ31B Magnesium Alloy

by L Farbaniec, CL Williams, L Kecskes, KT Ramesh, and R Becker

A reprint from International Journal of Impact Engineering. 2016;98:34–41.

Approved for public release; distribution is unlimited.

NOTICES

Disclaimers

The findings in this report are not to be construed as an official Department of the Army position unless so designated by other authorized documents.

Citation of manufacturer's or trade names does not constitute an official endorsement or approval of the use thereof.

Destroy this report when it is no longer needed. Do not return it to the originator.



Microstructural Effects on the Spall Properties of ECAE-Processed AZ31B Magnesium Alloy

by L Farbaniec and KT Ramesh

Johns Hopkins University, Baltimore, Maryland

Institute of Shock Physics, Imperial College London, London

CL Williams, L Kecskes, and R Becker

Weapons and Materials Research Directorate, ARL

A reprint from International Journal of Impact Engineering. 2016;98:34–41.

REPORT DOCUMENTATION PAGE				Form Approved OMB No. 0704-0188	
<p>Public reporting burden for this collection of information is estimated to average 1 hour per response, including the time for reviewing instructions, searching existing data sources, gathering and maintaining the data needed, and completing and reviewing the collection information. Send comments regarding this burden estimate or any other aspect of this collection of information, including suggestions for reducing the burden, to Department of Defense, Washington Headquarters Services, Directorate for Information Operations and Reports (0704-0188), 1215 Jefferson Davis Highway, Suite 1204, Arlington, VA 22202-4302. Respondents should be aware that notwithstanding any other provision of law, no person shall be subject to any penalty for failing to comply with a collection of information if it does not display a currently valid OMB control number.</p> <p>PLEASE DO NOT RETURN YOUR FORM TO THE ABOVE ADDRESS.</p>					
1. REPORT DATE (DD-MM-YYYY) October 2016		2. REPORT TYPE Reprint		3. DATES COVERED (From - To) January 2014–April 2016	
4. TITLE AND SUBTITLE Microstructural Effects on the Spall Properties of ECAE-Processed AZ31B Magnesium Alloy				5a. CONTRACT NUMBER	
				5b. GRANT NUMBER	
				5c. PROGRAM ELEMENT NUMBER	
6. AUTHOR(S) L Farbaniec, CL Williams, L Kecskes, KT Ramesh, and R Becker				5d. PROJECT NUMBER	
				5e. TASK NUMBER	
				5f. WORK UNIT NUMBER	
7. PERFORMING ORGANIZATION NAME(S) AND ADDRESS(ES) US Army Research Laboratory ATTN: RDRL-WMP-C Aberdeen Proving Ground, MD 21005-5069				8. PERFORMING ORGANIZATION REPORT NUMBER ARL-RP-0580	
9. SPONSORING/MONITORING AGENCY NAME(S) AND ADDRESS(ES)				10. SPONSOR/MONITOR'S ACRONYM(S)	
				11. SPONSOR/MONITOR'S REPORT NUMBER(S)	
12. DISTRIBUTION/AVAILABILITY STATEMENT Approved for public release; distribution is unlimited.					
13. SUPPLEMENTARY NOTES A reprint from International Journal of Impact Engineering. 2016;98:34–41.					
14. ABSTRACT Time-resolved normal plate impact experiments and spall recovery experiments were conducted to study the spall behavior of AZ31B-4E magnesium alloy processed via Equal-Channel Angular Extrusion (ECAE). The spall strength and incipient spall damage in the specimens were measured at different shock stresses using 51 mm and 105 mm bore gas guns. The Hugoniot Elastic Limit (HEL) was measured to be approximately 181 ± 3 MPa. The spall strengths extracted from the free surface velocity profiles of the shocked specimens were found to decrease by 5% for shock stresses ranging from 1.7 GPa to 4.6 GPa. However, this reduction in spall strength may fall within the experimental error. Post-test fractographic examinations of recovered specimens revealed that spall failure originated at micrometer-size intermetallic inclusions and propagated through the material by cavitation events with a very limited growth of voids. It was concluded that the strengthening of AZ31B-4E magnesium alloy by the ECAE-process resulted in adverse effects on its microstructure and spall behavior because of the process-induced cracking of intermetallic inclusions and their weak interface strengths.					
15. SUBJECT TERMS spall experiment, recovery experiment, microstructural characterizations, nucleation site, Mg alloys, magnesium, spall strength					
16. SECURITY CLASSIFICATION OF:			17. LIMITATION OF ABSTRACT UU	18. NUMBER OF PAGES 14	19a. NAME OF RESPONSIBLE PERSON L Farbaniec
a. REPORT Unclassified	b. ABSTRACT Unclassified	c. THIS PAGE Unclassified			19b. TELEPHONE NUMBER (Include area code) 410-278-8753



Microstructural effects on the spall properties of ECAE-processed AZ31B magnesium alloy



L. Farbaniec^{a,b,*}, C.L. Williams^c, L. Kecskes^c, K.T. Ramesh^{a,d}, R. Becker^c

^a Hopkins Extreme Materials Institute, Johns Hopkins University, Baltimore, MD 21218, USA

^b Institute of Shock Physics, Imperial College London, London SW7 2AZ, UK

^c U.S. Army Research Laboratory, Aberdeen Proving Ground, MD 21005, USA

^d Department of Mechanical Engineering, Johns Hopkins University, Baltimore, MD 21218, USA

ARTICLE INFO

Article history:

Received 29 April 2016

Received in revised form 26 July 2016

Accepted 1 August 2016

Available online 8 August 2016

Keywords:

Spall experiment

Recovery experiment

Microstructural characterizations

Nucleation site

Mg alloys

ABSTRACT

Time-resolved normal plate impact experiments and spall recovery experiments were conducted to study the spall behavior of AZ31B-4E magnesium alloy processed via Equal-Channel Angular Extrusion (ECAE). The spall strength and incipient spall damage in the specimens were measured at different shock stresses using 51 mm and 105 mm bore gas guns. The Hugoniot Elastic Limit (HEL) was measured to be approximately 181 ± 3 MPa. The spall strengths extracted from the free surface velocity profiles of the shocked specimens were found to decrease by 5% for shock stresses ranging from 1.7 GPa to 4.6 GPa. However, this reduction in spall strength may fall within the experimental error. Post-test fractographic examinations of recovered specimens revealed that spall failure originated at micrometer-size intermetallic inclusions and propagated through the material by cavitation events with a very limited growth of voids. It was concluded that the strengthening of AZ31B-4E magnesium alloy by the ECAE-process resulted in adverse effects on its microstructure and spall behavior because of the process-induced cracking of intermetallic inclusions and their weak interface strengths.

© 2016 Elsevier Ltd. All rights reserved.

1. Introduction

Magnesium (Mg) and its alloys have gained much attention for its potential in defense applications [1,2]. In part, this is because of their high strength-to-weight ratio and potential for further improvements in strength and ductility. Over the past few decades, many researchers have attempted to study the shock response of Mg in various forms, including single crystals, grain colonies, and Mg-based alloys [3–6]. These studies, however, focused on different research objectives. As such, the discussion of the mechanisms associated with the shock process, such as spall, was not thoroughly integrated with the post-test microstructural observations. Thus, further qualitative and quantitative studies of the Mg microstructures are needed to fully understand their response and behavior to shock loading (including spallation), and to establish the underlying processing–microstructure–property relationships.

Mg and its alloys have a hexagonal close-packed (hcp) crystal structure, and therefore, only a limited number of slip systems are available for deformation near room temperature. Effectively, this translates into poor formability and ductility. Of all the ways to

improve the dynamic strength and ductility of Mg and Mg alloys, Severe Plastic Deformation (SPD) techniques have gained much attention in recent years [7–12]. This is likely due to the fact that large-volume bulk samples of ultra-fine-grained materials can be produced at reasonable cost. Such fine-grained microstructures also exhibit high strengths while maintaining reasonable levels of ductility that, potentially, might improve the spall response of this class of materials.

A fundamental understanding of dynamic and shock deformation phenomena in Mg-based materials prior to the dynamic fracture and failure process became thus a key target of the manufacturing industry, leading to the development of advanced alloys with enhanced properties. These require systematic studies of pure Mg. In this context, for instance, Li [13] investigated the dynamic behavior of a Mg single crystal under $\langle c \rangle$ axis compression and found that the secondary pyramidal slip is the main deformation mechanism under dynamic compression loading. More recently, Dixit et al. [14] also studied dynamic deformation mechanisms of a Mg single crystal along the crystallographic $\langle a \rangle$ axis and found a large fraction of deformation twins of different variants under post-test microstructural characterizations. In other related studies, the shock response and spall strength of Mg single crystals have been measured in directions parallel and perpendicular to the $\langle c \rangle$ axis of the hcp structure and at 45° to the $\langle c \rangle$ axis [15,16]. These studies have shown that the Hugoniot elastic limit (HEL) is the largest for the material shocked along the $\langle c \rangle$ axis. Further, microstructural

* Corresponding author. Institute of Shock Physics, Imperial College London, London SW7 2AZ, UK. Fax: +44 (0)20 759 48955.

E-mail address: l.farbaniec@imperial.ac.uk (L. Farbaniec).

characterizations revealed intense twinning with a greater density of twins near the impact surface.

The formation of deformation twins under shock-loading was also observed and suggested in the case of polycrystalline Mg materials [6,17]. This phenomenon has also been observed in more systematic studies in the quasi-static and dynamic regimes, which revealed that the deformation twinning is strain rate sensitive as the fraction of twins increases under dynamic loading conditions [18–20]. Some other effects, such as temperature [5], texture [6] and grain size [21] on the spall strength of different Mg alloys, have been discussed in the existing literature. All were found to affect the spall strengths.

Many past studies have paid particular attention to AZ31B Mg alloys. Effects of texture and grain size on their dynamic response have been already studied at lower impact velocities by Asgari and co-workers [22,23]. It has been reported that their strong basal texture led to remarkable anisotropy of stress and strain. The later study [23] reported that the material with coarse grain microstructures exhibits a decrease in strength and ductility. Also, the total fraction of twins and strain hardening rate increase with larger grain sizes. The spall behavior of AZ31B Mg alloy has also been studied in the past years [3,4]. For example, Schmidt et al. [4] studied the temperature dependent spall threshold of AZ31B-H24 Mg alloy and reported spall strength values of approximately 1.5 GPa near room temperature, and approximately 0.2 GPa near the solidus or the melting point. McQueen et al. [3] estimated the spall strength of AZ31B Mg alloy from the free surface velocity profiles to be approximately 0.8 GPa.

In this paper, we aim to investigate the spall properties of AZ31B-4E Mg alloy, where '4E' stands for a hybrid route in the Equal-Channel Angular Extrusion (ECAE) process. The ECAE process results in an overall improvement of strength and hardness while still resulting in an acceptable ductility level. Such properties are especially desirable in dynamic applications. To this end, we aim to identify the spallation mechanisms with respect to the processing–microstructure–properties relationship.

2. Experimental procedure

2.1. Equal-channel angular extrusion

A rectangular Mg alloy (AZ31B-H24) plate with the dimensions of 152.4 mm × 152.4 mm and a thickness of 12.7 mm was extruded by ECAE through a die using a hybrid 4E route. The 4E route implies that the plate was rotated about the plate normal 180° after the first pass, 90° after the second pass, and 180° after the third pass, and extruded through the die for a total of four passes. The plate processing temperature was varied from 498 K during the first two passes then was dropped to 473 K on the last two passes. The extrusions were performed with a back pressure ranging from 4.14 kPa to 6.89 kPa and the extrusion speed was 4.6 mm/min. The nominal grain size resulting from this ECAE process and for this Mg alloy is approximately 3 μm. Plate impact specimens were fabricated using wire electro-discharge machining from the through-thickness direction of the plate (which is also the shock direction). Listed in Table 1 are the measured density and wave speeds from which the

elastic constants were calculated. The values listed in Table 1 are consistent with those found in the open literature.

2.2. Plate impact experiments

Shock experiments were conducted using a single stage 51 mm (smooth bore) and 102 mm (slotted bore) diameter gas guns at the U.S. Army Research Laboratory (ARL, Aberdeen Proving Ground). The 51 mm diameter gun was used for impact velocities equal to or less than 700 m/s and the 102 mm diameter gun for velocities greater than 700 m/s. Both, in-situ (real-time) spall and ex-situ (end-state) recovery experiments were conducted using the standard plate impact technique. The basic loading configuration was previously described by Williams and co-workers [24–26]. For this investigation, all plate impact experiments were symmetric, that is, both the flyer and target materials were identical. The nominal diameter of the specimen for the spall experiments was approximately 42 mm and the thickness was approximately 6 mm. The flyer had a nominal diameter and thickness of 42 mm and 3 mm, respectively. Spall recovery specimens were 3 mm thick and 19 mm in diameter. The flyer had a nominal diameter and thickness of 42 mm and 2 mm, respectively. A series of charged pins were used to determine the flyer velocity and the uncertainty associated with the pin positions was determined to be less than 1.0×10^{-4} mm, corresponding to an error associated with the final velocity of the flyer of less than 2%. Using laser alignment, the tilt was determined to be normal to within 0.5 mrad. The free surface velocity–time histories were acquired using Photonic Doppler Velocimetry (PDV) from which the corrected spall strengths were calculated.

2.3. Characterization techniques

A typical specimen used in the plate impact experiments (unshocked) was metallographically prepared to study the microstructure of the as-processed material. The investigation was performed in the plane of the specimen, which is normal to the shock direction (the through-thickness direction of the plate). The metallographic preparation process involved mechanical polishing using 1200 (P-4000) grit SiC paper, which was followed by final polishing with a 0.05 μm colloidal silica suspension. Subsequently, in order to remove damaged surface layers caused by the mechanical polishing, the sample was ion-milled using a Fischione 1060 SEM Mill ion-milling system at 4.5 keV ion beam energy for 5 minutes with a 2° specimen tilt angle.

Microstructure analysis was performed using a TESCAN MIRA3 field emission Scanning Electron Microscope (SEM) equipped with a fully automated electron backscatter diffraction (EBSD) analysis system and Energy Dispersive Spectroscopy (EDS) capabilities. The resulting EBSD maps were analyzed with the OIM™ software from TexSem Laboratories (TSL). The EBSD analysis was performed with a step size of 0.1 μm. The secondary phases were not the subject of interest in this study. The chemical analysis of the specimen was carried out with an operating voltage of 15 keV and a minimum spot size of 0.8 μm. The TEAM™ software (EDAX, Inc.) was used in the chemical characterization of the specimen.

Table 1
Measured wave velocities and calculated elastic constants (based on 5 measurements).

	Measured thickness t [mm]	Measured diameter d [mm]	Long. wave speed C_L [km/s]	Shear wave speed C_S [km/s]	Density ρ [kg/m ³]	Bulk modulus K [GPa]	Lame's constant λ [GPa]	Elastic modulus E [GPa]	Shear modulus μ [GPa]	Poisson ratio ν
Average	5.890	41.938	5.820	3.065	1773.750	37.867	26.758	43.596	16.664	0.308
Std. Dev.	0.007	0.008	0.020	0.009	5.355	0.218	0.211	0.136	0.054	0.001

The shock-recovered specimens were carefully sectioned (parallel and perpendicular to the axis of the specimen) and metallographically prepared for the SEM examination. A Leica Microsystems optical microscope was also used to image the cross-sections of the shocked specimens.

3. Microstructure

The elemental constituents of the as-processed material were determined by the EDS technique. Fig. 1 shows a typical EDS spectrum of a larger ($\sim 1 \text{ mm}^2$) representative area of the specimen. It shows a major peak of Mg (balance) with a detectable amount of Al, Zn, Mn and few other elements. A list of elements identified and their atomic concentration (at.%) is also presented. The resultant composition is in good agreement with other AZ31B Mg alloys, for example see Ref. [27].

Fig. 2a shows a typical EBSD map collected from the (unshocked) specimen in the plane normal to the shock direction (for reference, see the schematic drawing of the specimen). The microstructure is composed of submicrometer-sized grains with a presence of a crystallographic texture. The corresponding pole figure of the mapped grains is shown in Fig. 2b. Use of this ECAE processing route resulted in the development of a strong $\langle 0001 \rangle$ fibre texture component (6–7 times random) parallel to the direction of the impact. The fibre texture is not ‘perfect’ as there is not normally distributed scatter about the ideal orientation. The grain-size distribution as obtained from the EBSD analysis is presented in Fig. 2c. The grain size range is small (0–6 μm) and can be fitted by a log-normal function. The arithmetic and the area-weighted mean grain sizes were measured to be $1.35 \pm 0.77 \mu\text{m}$ and $2.34 \pm 1.28 \mu\text{m}$, respectively. Such microstructural characteristics, with regards to texture and grain sizes, are very common for hcp materials fabricated via SPD processing routes [27].

Fig. 3(a–c) show SEM micrographs at increasing magnifications of the (unshocked) specimen in backscattered electron contrast (BSE) mode. Note that BSE mode provides phase contrast based on composition variation. Thus, the brighter area in the image corresponds to a higher atomic number material. As in previous experiments, the images were taken on the surface of the specimen that lies in the plane normal to the shock direction (for reference, see the schematic drawing of the specimen with the attached coordinate system). Fig. 3a shows the investigated specimen with the

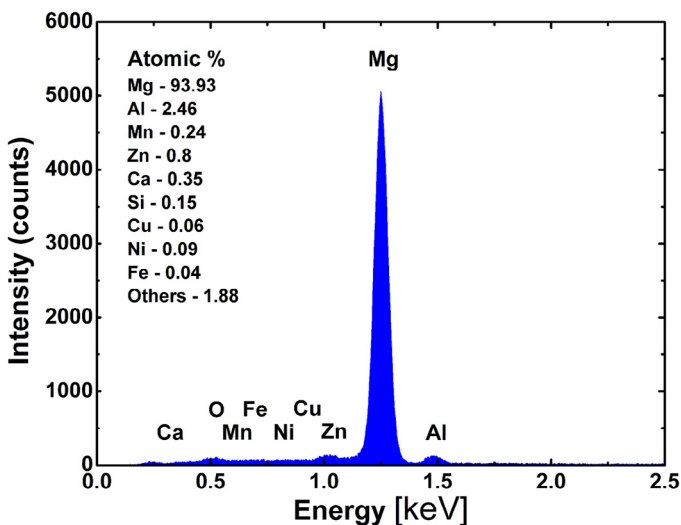


Fig. 1. SEM/EDS spectrum of the AZ31B-4E Mg alloy. A list of identified elements and their atomic concentration (at.%) are included.

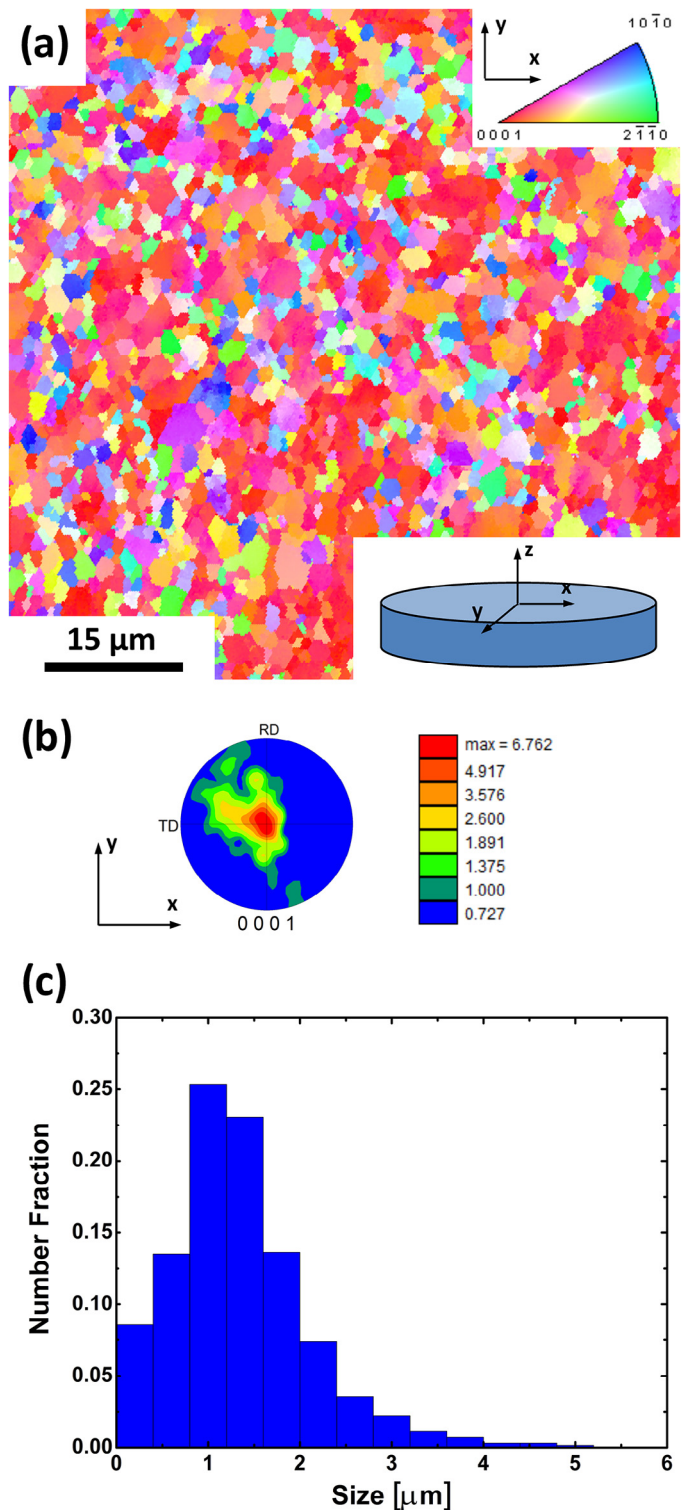


Fig. 2. Microstructure characteristics of the AZ31B-4E Mg alloy: (a) inverse pole figure map; (b) local texture variation; (c) grain size distribution.

area of interest boxed and shown at higher magnification in Fig. 3b. The presence of secondary phases in the material is prominent. These secondary phases are irregular in shape, heterogeneous in size, and rather uniformly spread in the material over distances of the order of tens of micrometers. It is difficult to develop an accurate quantitative analysis of the precipitate distribution because of the complex morphology of the sometimes clustered and fragmented precipitates.

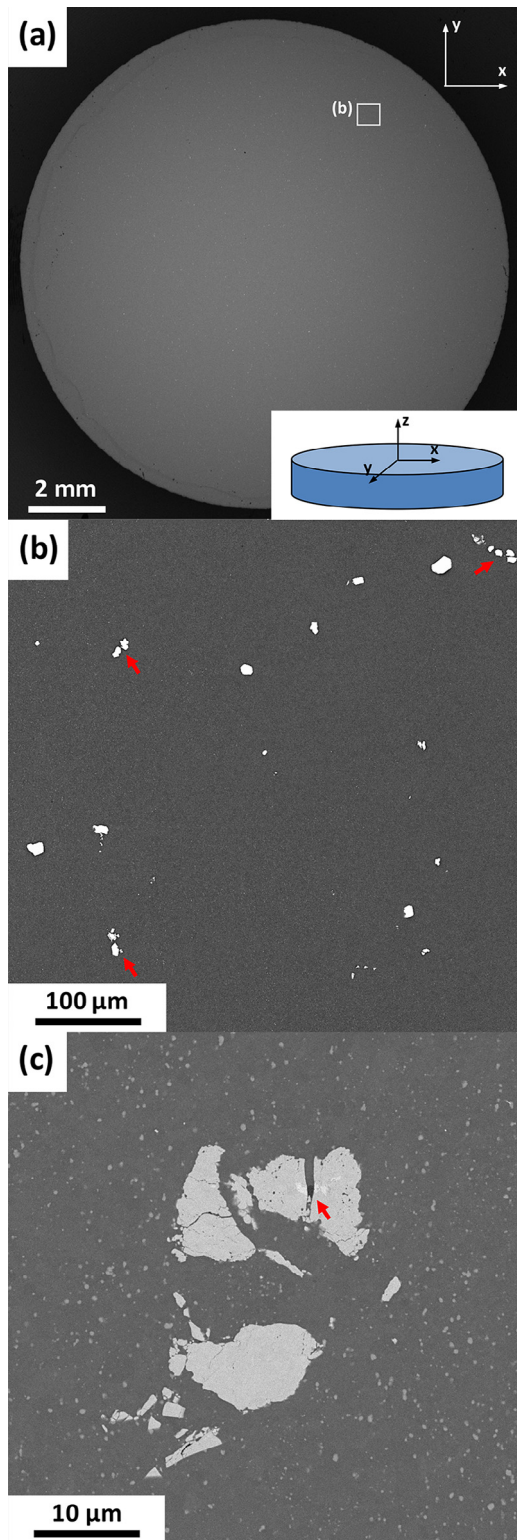


Fig. 3. SEM micrographs of the unshocked specimen in backscattered electron contrast (BSE) mode, where: (a) investigated specimen; (b) zoomed-in investigated surface with indicated secondary phases; (c) high-magnification observations of the specimen showing a cluster of broken secondary phases and precipitates responsible for strengthening in this alloy.

Also, it is challenging to separate the population of broken Al-Mn inclusions from submicron-sized strengthening particles using standard image-processing technique. That said, the average spacing between the secondary phases was estimated to be approximately

65 μm . Note that the distance between phases is much greater than the area investigated by the EBSD technique. Moreover, these phases are often arranged in clusters (indicated by the arrows in Fig. 3b). A more detailed investigation at higher magnification of such cluster of secondary phases is shown in Fig. 3c. As revealed by the figure, it is a rather discontinuous streak of broken fragments formed as a consequence of the ECAE processing route. The shape of these fragments suggests that they are likely brittle, and the lack of BSE contrast indicates that they are rather homogeneous in chemical composition. The presence of brittle inclusions in light alloys and metals is a major problem for most Severe Plastic Deformation (SPD) processes. For example, Whelchel et al. [28] studied the spall response of Al 5083 fabricated by combined equal-channel angular pressing (ECAP) and rolling, and found that the spall strength of the material decreased due to the cracking of inclusions caused by the cold rolling.

Note that some previous studies on AZ31B Mg alloys have also reported the existence of intermetallic phases [29,30]. These phases have been identified as uniform, round to oval in shape, and ranging in size from a few to several micrometers in diameter. Therefore, the present study has revealed certain limitations of using the ECAE technique for this Mg alloy. That is to say, if the material is composed of large brittle inclusions, and is exposed to the ECAE process, there is a strong likelihood that these inclusions will break down and, thus, potentially introduce weak interfaces to the material. Such an example of a broken down inclusion acting as a weak interface (much like a void would) is indicated by an arrow in Fig. 3c (such inclusions with sharp interfaces provides stress raisers). These findings might have important implications for understanding shock deformation processes undergoing in this ECAE-processed Mg alloy. This is because the pre-existing voids might act as spall nucleation sites when the incident compressive and reflected tensile waves interact.

Fig. 3c also shows the degree of precipitation strengthening in the material. This is manifested through a uniform distribution of closely spaced submicron-sized particles throughout the alloy. The function of such precipitates is to impede dislocation motion through the alloy and thus improve the strength of the material. The observed precipitates are believed to have different chemistry than the large secondary phases due to the slightly different BSE contrast.

Fig. 4 presents the results of the EDS analysis of a typical precipitate cluster of the secondary phases and the surrounding AZ31B alloy material, where the SEM micrograph of the investigated area is presented in Fig. 4a, and elemental maps of Mg, Mn, Al, Fe and Zn are presented in Fig. 4(b–f), respectively. The large phases appear to be intermetallic and composed of Al, Mn and to a lesser extent Fe, as deduced from Fig. 4(c–e). In contrast, based on the elemental maps, Al and Zn are more likely concentrated in the smaller precipitates. However, it is not possible to determine the true composition of the small precipitates. This is due to the inherent limited resolution of the EDS analysis (0.8 μm of the sampling area size).

The investigated cluster of secondary phases, similar to that shown in Fig. 3c, has an internal void of considerable size (indicated by the arrow in Fig. 4a). It is assumed that this is a void because the corresponding EDS map of Mg (Fig. 4b) does not reveal much evidence of elemental Mg in this area (compare the area indicated by the arrows in Fig. 4(a–b)). It should be noted here that such voids near the intermetallic inclusions were not very common at sub-micron scale (there were only a few examples on the investigated surface of the specimen). More detailed and more in depth observations would be useful. For example, examination using Transmission Electron Microscopy (TEM) would provide better opportunities, wherein, the interfaces between these phases and the alloy material might be seen in much more detail to confirm the weakening effect of nanovoids.

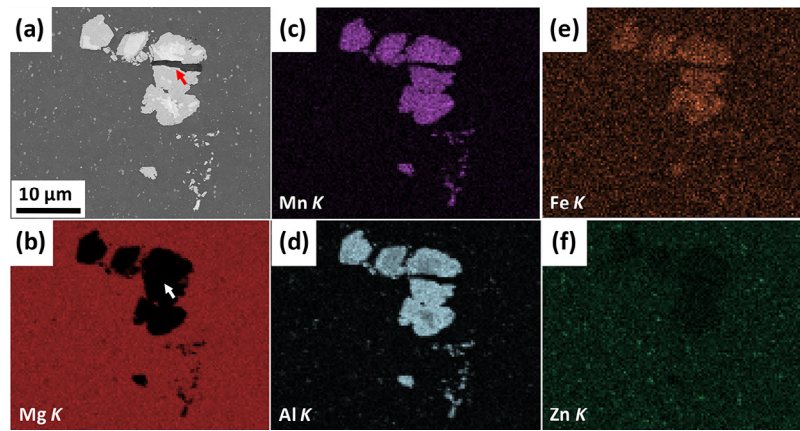


Fig. 4. Combined SEM/EDS map analysis of the AZ31B-4E Mg alloy, where: (a) SEM micrograph of the investigated area; (b) EDS elemental map of Mg; (c) EDS elemental map of Mn; (d) EDS elemental map of Al; (e) EDS elemental map of Fe; (f) EDS elemental map of Zn.

4. Spall response

Fig. 5 shows the velocity-time profiles of the free surface motion of the shocked samples at different impact velocities. The origin of the time axis corresponds to the arrival times of the elastic precursor at the rear surface. The average peak free surface velocities measured by PDV were 391.0 ± 1.6 m/s, 571.8 ± 2.6 m/s, 848.1 ± 0.9 m/s, and 995.0 ± 2.5 m/s, respectively. These correspond to shock stresses of 1.68 GPa, 2.51 GPa, 3.86 GPa, and 4.60 GPa, respectively. All free surface velocity profiles in Fig. 5 show an elastic precursor wave that is followed by a plastic shock wave. Such profiles are characteristic of elastic-plastic materials undergoing shock compression, release, and spall. The nominal HEL determined from the velocity-time profiles is approximately 181 ± 3 MPa.

The spall pulses in the free surface velocity profiles are well defined (indicated by the black arrows). These appear as a consequence of void nucleation, growth, and coalescence inside the specimens. The spall fracture is initiated due to the interaction between reflecting tensile waves. If the resulting tensile stress in the specimen meets the threshold for void nucleation, growth, and coalescence, then spall fracture can initiate inside the specimen. The

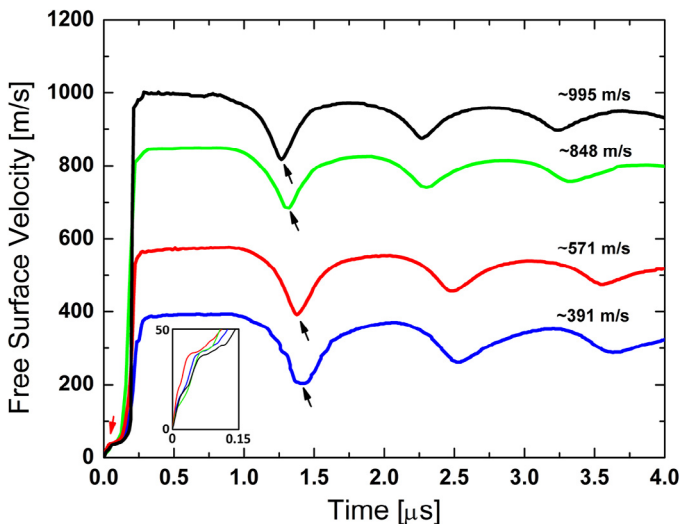


Fig. 5. Free surface velocity profiles measured in the specimens shock-compressed at the impact velocities of approximately 391 m/s (blue), 571 m/s (red), 848 m/s (green), and 995 m/s (black). The spall pulses are indicated by the black arrows. The inset is an enlargement of the Hugoniot elastic limit area (indicated by the red arrow) in the velocity profiles.

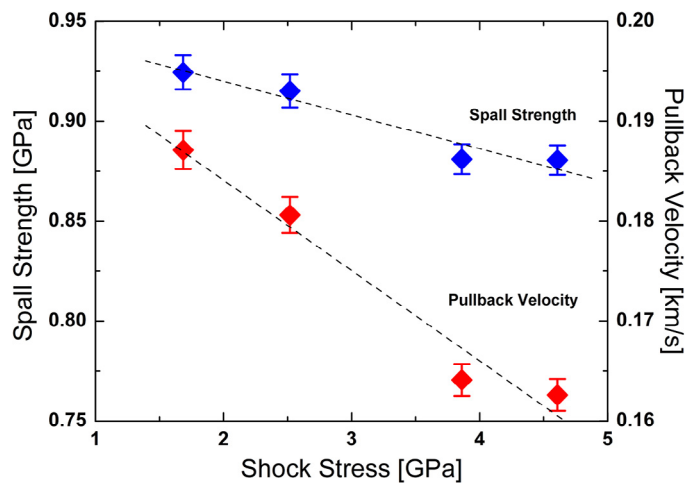


Fig. 6. Spall response and pullback velocities of the shock-compressed specimens.

velocity pullback (the difference between the maximum velocity at the Hugoniot state and the minimum velocity before the spall pulse), which is an indirect stress measurement through the momentum equations, is used for calculating the spall strength.

Fig. 6 presents the pullback velocity and the corrected spall strengths as a function of shock stress. Note that the correction for the spall strength was calculated in accordance with Ref. [31] to account for elastic-plastic effects. The results show a reduction in the pullback velocity as a function of shock stress. More precisely, a ~15% decrease of this property was found as the shock stress increases from approximately 1.7 GPa to 4.6 GPa. The observed reduction in spall strength (~5%) is smaller for the investigated shock stresses, and more spall experiments are needed at higher shock stresses to confirm the reduction in spall strength. Further experimental efforts, however, should be coordinated with spall simulations for a better understanding of the interacting waves.

Also, it should be noted that the corrected spall strengths reported in this study for the ECAE-processed AZ31B Mg alloy (AZ31B-H24 Mg alloy as starting material) are lower than the spall strength value (1.5 GPa at room temperature¹) reported for AZ31B-H24 Mg alloy in Schmidt et al. [4], for example. Despite the possible

¹ In Ref. [4], the method applied for calculating the spall strength is described with a lack of details. Note that the spall strength reported in our study is corrected to account for elastic-plastic effects [31].

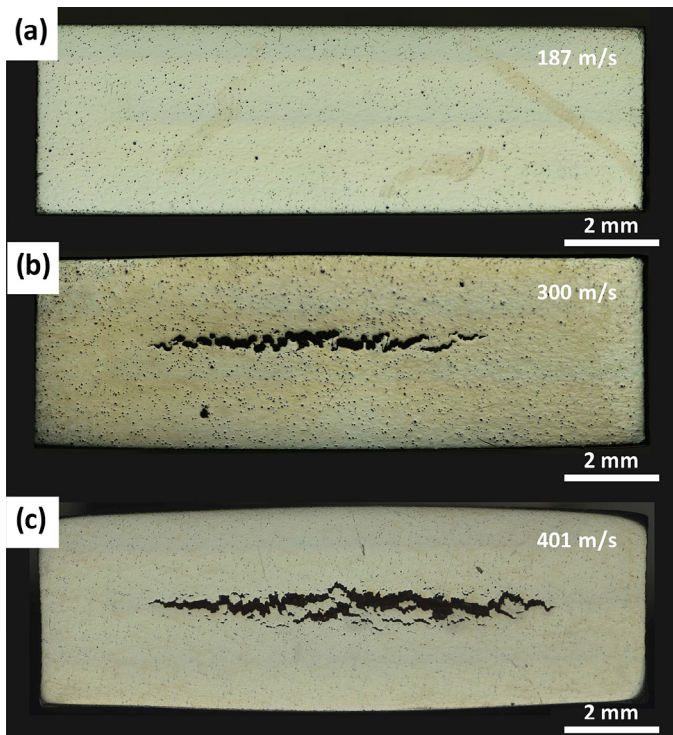


Fig. 7. Optical micrographs of the cross-sections of the specimens shocked at 187 m/s, 300 m/s and 401 m/s.

differences in the microstructure of these two AZ31B Mg alloys, and what follows potential variations in the spall strengths, the lower values of the resistance to spall fracture shown by the ECAE-processed material are most likely to be associated with the processing technique. In order to understand the material undergoing spallation or spall failure, further plate impact recovery experiments have been performed, which have been followed by post-test fractography. These are as discussed in the next section.

5. Failure mechanisms

Spall recovery experiments were used to initiate incipient spallation damage in the specimens. These experiments were performed

at velocities ranging from 100 m/s to 400 m/s. Fig. 7 shows the optical micrographs of the cross-sections of the specimens shocked at 187 m/s, 300 m/s, and 401 m/s, respectively. Post-mortem examination of the recovered specimens showed no obvious visual evidence of damage up to 187 m/s. However, higher velocity spall recovery experiments revealed a well-developed spall plane in the specimen. Therefore, it may be surmised that for this Mg alloy the threshold velocity for spallation lies within the range 187–300 m/s, and the damaged volume extends farther from the spall plane for the higher velocity impacts.

Fig. 8(a–d) show the SEM results of the specimen shocked at 401 m/s. An overall view of the damage zone in the specimen is presented in Fig. 8a. The spall can be characterized as having multiple failure planes (with one dominant principal plane), which are independent of each other at the early stage of spallation. The principal spall plane is rather rough, and suggests that the microstructure and its intrinsic substructural inhomogeneities play an important role in this failure process. This is especially true for large intermetallic inclusions, which create interfaces with respect to the soft matrix Mg, in turn, being a source of weakness. Indeed, there are numerous examples where voids nucleate from clusters of inclusions in the vicinity of the spall plane. Such well-developed voids surrounded by the large intermetallic inclusions (indicated by the arrows) are presented in Fig. 8b. These voids initiate near the center of the particle fragment cluster (such as the one in Fig. 3c), and their growth direction and shapes are rather complex. The following subfigures show the same type of inclusions near the edge of the spall plane and inside the spall plane. Fig. 8c, for example, shows the presence of inclusions (indicated by the arrows) near the edge of the principal spall plane, which was taken at the location indicated in Fig. 8a. Note the similarity in shape and size between the inclusions presented in Fig. 8b and Fig. 8c. These were common observations in this cross section plane all along the damage zone and inside the spall planes. Fig. 8d shows such a broken intermetallic inclusion on the fracture surface inside the principal spall plane. Its location is indicated in Fig. 8a. Interestingly, note the presence of nanovoids on the surface of the inclusion (as indicated by the enlarged view of the area boxed in Fig. 8d). These nanovoids likely form within the *matrix* Mg which is in direct contact with the intermetallic inclusions. These are discussed in more detail later in this section. Further analysis of the inclusions on the fracture surface is facilitated by sectioning the specimen parallel to the spall plane.

Fig. 9a shows the SEM micrograph of the same specimen (shocked at 401 m/s) polished down to approximately one-half of its thickness. The following areas of interest are indicated in this figure by

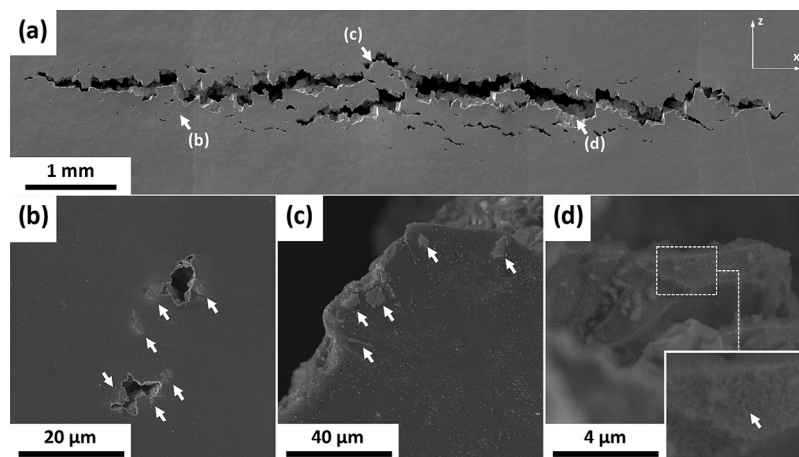


Fig. 8. SEM investigation (BSE mode) of the cross-section of the recovered specimen shocked at 401 m/s: (a) closer view of the damage zone showing multiple spall planes; (b) spall formation and void growth originating from the clusters of inclusions in the vicinity of the spall plane (the inclusions are indicated by the arrows); (c) intermetallic inclusions at the edge of the spall plane; (d) intermetallic inclusions inside the spall plane.

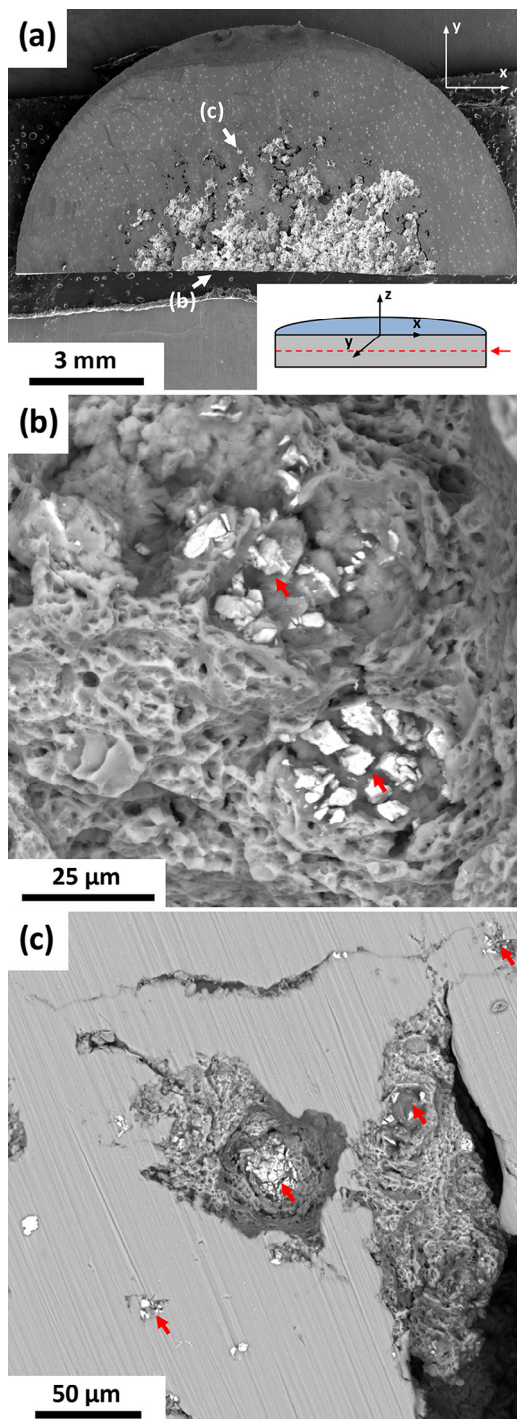


Fig. 9. SEM investigation (BSE mode) of the mid-plane (spall plane) of the recovered specimen shocked at 401 m/s: (a) investigated specimen (the red arrow in the schematic drawing indicates the position of the plane of the specimen under investigation); (b) zoomed-in fracture surface at the center of the spall plane with intermetallic inclusions indicated; (c) zoomed-in fracture surface at the edge of the spall plane with intermetallic inclusions indicated.

the arrows and shown at higher magnification in Fig. 9(b–c). The view is in the direction normal to the spall plane (see the schematic drawing of the sample). Note that the spall surface is not planar and, consequently, the fracture surface is at various distances from the polished surface. A more detailed investigation at higher magnification of the damage zone confirmed that the large intermetallic inclusions play a crucial role in the failure process. Fig. 9b shows the fracture surface

of the specimen in the center of the spall plane. Two clusters of inclusions are indicated by the arrows. Similar clusters of inclusions were observed at the outer regions of the sample (Fig. 9c). It is likely that these clusters of inclusions were formed during the ECAE process (when compared with Fig. 3c) and not as a result of the void growth (or spall plane expansion). Nevertheless, their locations on the fracture surface, and probably most important their prevalence, suggest that these inclusions act as initiation sites for spall failure.

In addition, particular attention must be given to the fact that a vast majority of the fracture surface is populated by submicron-sized voids. See, for example, Fig. 9b that shows widespread dimples over the fracture surface. It is generally assumed that such dimples are formed due to void nucleation from either particle cracking or debonding of the particle–matrix interface. The SEM observations, however, showed no direct evidence for the formation of these very small voids at the previously-discussed intermetallic inclusions. It is most likely that they are formed at strengthening precipitates, which are commonly reported (as in Fig. 3c). This assumption is based on observations that the strengthening precipitates were frequently reported on the fracture surfaces. However, some other mechanisms, such as shock-induced vacancy generation and clustering that potentially are followed by nanovoid growth [32,33], might also be taken into consideration under these loading conditions.

In the discussion related to Fig. 8d, which concerned the investigation of the cross-sections of the specimens, we reported the formation of nanovoids on the fracture surfaces (Fig. 8d). These observations were confirmed in the direction normal to the spall plane. Fig. 10 shows the SEM micrograph of such a fracture surface in the center of the spall plane with the enlarged view of the boxed area. These nanovoids seem to be nucleated near the interface between the intermetallic inclusions and the matrix Mg. Therefore, assuming that the spall failure initiated at these locations, the nanovoids appear to be the main causative factor or ‘actor’ at the early stage of spallation. All these make the spallation mechanisms more complicated, because even the damage near the intermetallic inclusions has a separate, lower-scale mechanism.

Finally, this paper sought to develop the processing–microstructure–property relationship. In this context, one could assume that the ECAE technique can provide a fine-grained material with mechanically enhanced properties. This is particularly true for pure metals. In the case of AZ31B–H24 Mg alloy, however, the ECAE-process resulted in a significant grain refinement (as expected), but also in deterioration of

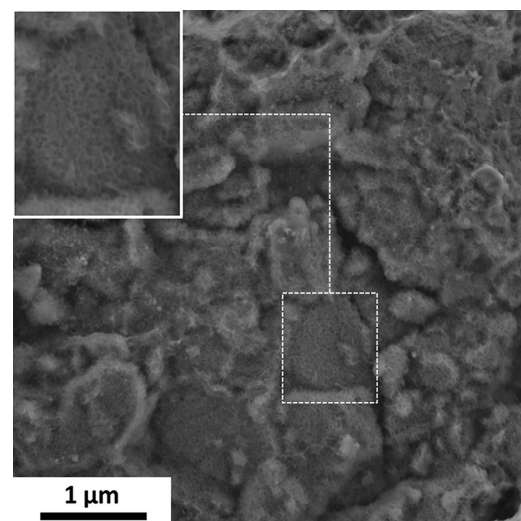


Fig. 10. SEM micrograph of the fracture surface in the center of the spall plane showing the appearance of nanovoids at the interface between the intermetallic inclusions and the matrix of the alloy material.

the microstructure through the cracking of pre-existing intermetallic inclusions. The streak of broken inclusions had a negative impact on the spall behavior of this material. Therefore, there should be more effort put into the processing of Mg alloys to avoid the formation of large intermetallic inclusions.

6. Summary

The spall behavior of AZ31B–4E Mg alloy, where ‘4E’ stands for a hybrid route in the Equal-Channel Angular Extrusion (ECAE) process, was investigated by normal plate impact and plate impact recovery experiments. The results showed that the spall strengths decreased by 5% for shock stresses ranging from 1.7 GPa to 4.6 GPa. However, this decrease in spall strength may fall within the experimental error and therefore, more experiments at higher shock stresses are needed to validate this trend. The Hugoniot Elastic Limit (HEL) was found to be $\sim 181 \pm 3$ MPa. The microstructure before and after the tests was characterized using scanning electron microscopy-based characterization techniques (SEM/EDS/EBSD). It was shown that this Mg alloy has a fine-grained microstructure with the presence of a strong crystallographic texture. The material is also populated with numerous fragmented intermetallic inclusions and closely spaced submicrometer-sized precipitates. These microstructural defects (particular emphasis is placed on fragmented intermetallic inclusions) are most likely responsible for the initiation of spall in the shocked specimen. Based on fractographic examinations, it is also hypothesized that the early stage of the spallation is dominated by nanovoid formation near the interfaces between the intermetallic inclusions and the alloy material (the *matrix* Mg).

Acknowledgments

The authors gratefully acknowledge Dr. Brian Schuster and Dr. Mike Zellner for their technical support with PDV coverage. Also, the authors wish to acknowledge Mr. Jermaine Bradley, Mr. Micah Gallagher, Mr. Ron Worthington, and Mr. Eric Wilson for their valuable technical support.

This work was sponsored by the Army Research Laboratory and was accomplished under Cooperative Agreement Number W911NF-12-2-0022. The views and conclusions contained in this document are those of the authors and should not be interpreted as representing the official policies, either expressed or implied, of the Army Research Laboratory or the U.S. Government. The U.S. Government is authorized to reproduce and distribute reprints for Government purposes notwithstanding any copyright notation herein.

Approved for public release; distribution is unlimited.

References

- [1] Clow B. Magnesium: the lightest one. In: Wells M, Kula E, Beatty J, editors. *Metallic materials for lightweight applications: proceedings of the 40th Sagamore Army Materials Research Conference*. Washington, DC: Government Printing Office; 1993. p. 235–9.
- [2] Jones T, Kondoh K. Initial evaluation of advanced powder metallurgy magnesium alloys for dynamic applications, US Army Research Laboratory Technical Report, ARL-TR-4828, 2009.
- [3] McQueen R, Marsh S, Taylor J, Fritz J, Carter W. Chapter vii: the equation of state of solids from shock wave studies. In: Kinslow R, editor. *High-velocity impact phenomena*. New York: Academic Press; 1970. p. 293–417.
- [4] Schmidt R, Davies F, Lempriere B, Holsapple K. Temperature dependent spall threshold of four metal alloys. *J Phys Chem Solids* 1978;39(4):375–85. doi:10.1016/0022-3697(78)90079-3.
- [5] Kanel G, Razorenov S, Bogatch A, Utkin A, Grady DE. Simulation of spall fracture of aluminum and magnesium over a wide range of load duration and temperature. *Int J Impact Eng* 1997;20(6):467–78. doi:10.1016/s0734-743x(97)87435-0. [http://dx.doi.org/10.1016/s0734-743x\(97\)87435-0](http://dx.doi.org/10.1016/s0734-743x(97)87435-0).
- [6] Hazell P, Appleby-Thomas G, Wielewski E, Stennett C, Siviour C. The influence of microstructure on the shock and spall behaviour of the magnesium alloy, Elektron 675. *Acta Mater* 2012;60(17):6042–50. doi:10.1016/j.actamat.2012.07.041.
- [7] Mabuchi M, Iwasaki H, Yanase K, Higashi K. Low temperature superplasticity in an az91 magnesium alloy processed by ecae. *Scr Mater* 1997;36(6):681–6. doi:10.1016/s1359-6462(96)00444-7.
- [8] Yamashita A, Horita Z, Langdon TG. Improving the mechanical properties of magnesium and a magnesium alloy through severe plastic deformation. *Mater Sci Eng A* 2001;300(1):142–7. doi:10.1016/s0921-5093(00)01660-9.
- [9] Kim W, Hong S, Kim Y, Min S, Jeong H, Lee J. Texture development and its effect on mechanical properties of an az61 mg alloy fabricated by equal channel angular pressing. *Acta Mater* 2003;51(11):3293–307. doi:10.1016/s1359-6454(03)00161-7.
- [10] Agnew S, Horton J, Lillo T, Brown D. Enhanced ductility in strongly textured magnesium produced by equal channel angular processing. *Scr Mater* 2004;50(3):377–81. doi:10.1016/j.scriptamat.2003.10.006.
- [11] Agnew S, Mehrotra P, Lillo T, Stoica G, Liaw P. Texture evolution of five wrought magnesium alloys during route a equal channel angular extrusion: experiments and simulations. *Acta Mater* 2005;53(11):3135–46. doi:10.1016/j.actamat.2005.02.019.
- [12] Figueiredo RB, Száraz Z, Trojanová Z, Lukáč P, Langdon TG. Significance of twinning in the anisotropic behavior of a magnesium alloy processed by equal-channel angular pressing. *Scr Mater* 2010;63(5):504–7. doi:10.1016/j.scriptamat.2010.05.016.
- [13] Li Q. Dynamic mechanical response of magnesium single crystal under compression loading: experiments, model, and simulations. *J Appl Phys* 2011;109(10):103514. doi:10.1063/1.3585870.
- [14] Dixit N, Hazeli K, Ramesh KT. Twinning in magnesium under dynamic loading. *EPJ Web Conf* 2015;94:02018. doi:10.1051/epjconf/20159402018.
- [15] Kanel G, Garkushin G, Savinykh A, Razorenov S, de Resseguier T, Proud W, et al. Shock response of magnesium single crystals at normal and elevated temperatures. *J Appl Phys* 2014;116(14):143504. doi:10.1063/1.4897555.
- [16] Winey J, Renganathan P, Gupta Y. Shock wave compression and release of hexagonal-close-packed metal single crystals: inelastic deformation of c-axis magnesium. *J Appl Phys* 2015;117(10):105903. doi:10.1063/1.4914525.
- [17] Millett J, Stirk S, Bourne N, Gray G. On the behaviour of the magnesium alloy, az61 to one-dimensional shock loading. *Acta Mater* 2010;58(17):5675–82. doi:10.1016/j.actamat.2010.06.042.
- [18] Tucker M, Horstemeyer M, Gullett P, El Kadiri H, Whittington W. Anisotropic effects on the strain rate dependence of a wrought magnesium alloy. *Scr Mater* 2009;60(3):182–5. doi:10.1016/j.scriptamat.2008.10.011.
- [19] Ahmad I, Shu D. Compressive and constitutive analysis of az31b magnesium alloy over a wide range of strain rates. *Mater Sci Eng A* 2014;592:40–9. doi:10.1016/j.msea.2013.10.056.
- [20] Dixit N, Xie KY, Hemker KJ, Ramesh K. Microstructural evolution of pure magnesium under high strain rate loading. *Acta Mater* 2015;87:56–67. doi:10.1016/j.actamat.2014.12.030.
- [21] Asgari H, Szpunar J, Odeshi A, Zeng L, Olsson E. Effect of grain size on high strain rate deformation of rolled mg–4y–3re alloy in compression. *Mater Sci Eng A* 2015;633:92–102. doi:10.1016/j.msea.2015.03.020.
- [22] Asgari H, Szpunar J, Odeshi A, Zeng L, Olsson E. Experimental and simulation analysis of texture formation and deformation mechanism of rolled az31b magnesium alloy under dynamic loading. *Mater Sci Eng A* 2014;618:310–22. doi:10.1016/j.msea.2014.09.043.
- [23] Asgari H, Odeshi A, Szpunar J, Zeng L, Olsson E. Grain size dependence of dynamic mechanical behavior of az31b magnesium alloy sheet under compressive shock loading. *Mater Charact* 2015;106:359–67. doi:10.1016/j.matchar.2015.06.030.
- [24] Williams C, Ramesh K, Dandekar D. Spall response of 1100-o aluminum. *J Appl Phys* 2012;111(12):123528. doi:10.1063/1.4729305.
- [25] Williams C, Chen C, Ramesh K, Dandekar D. The effects of cold rolling on the microstructural and spall response of 1100 aluminum. *J Appl Phys* 2013;114(9):093502. doi:10.1063/1.4817844.
- [26] Williams C, Chen C, Ramesh K, Dandekar D. On the shock stress, substructure evolution, and spall response of commercially pure 1100-o aluminum. *Mater Sci Eng A* 2014;618:596–604. doi:10.1016/j.msea.2014.09.030.
- [27] Gzyl M, Pesci R, Rosochowski A, Boczkal S, Olejnik L. In situ analysis of the influence of twinning on the strain hardening rate and fracture mechanism in az31b magnesium alloy. *J Mater Sci* 2015;50(6):2532–43. doi:10.1007/s10853-014-8812-0.
- [28] Whelchel R, Thadhani N, Sanders T, Kecskes L, Williams C. Spall properties of al 5083 plate fabricated using Equal-Channel Angular Pressing (ECAP) and rolling. *J Phys Conf Ser* 2014;500:112066. doi:10.1088/1742-6596/500/11/112066. IOP Publishing.
- [29] Lin X, Chen D. Strain controlled cyclic deformation behavior of an extruded magnesium alloy. *Mater Sci Eng A* 2008;496(1):106–13. doi:10.1016/j.msea.2008.05.016.
- [30] Chowdhury S, Chen D, Bhole S, Cao X, Powidajko E, Weckman D, et al. Tensile properties and strain-hardening behavior of double-sided arc welded and friction stir welded az31b magnesium alloy. *Mater Sci Eng A* 2010;527(12):2951–61. doi:10.1016/j.msea.2010.01.031.
- [31] Kanel G. Distortion of the wave profiles in an elastoplastic body upon spalling. *J Appl Mech Tech Phys* 2001;42:358–62. doi:10.1023/A:1018804709273.
- [32] Reina C, Marian J, Ortiz M. Nanovoid nucleation by vacancy aggregation and vacancy-cluster coarsening in high-purity metallic single crystals. *Phys Rev B* 2011;84(10):104117. doi:10.1103/physrevb.84.104117.
- [33] Wilkerson J, Ramesh K. A closed-form criterion for dislocation emission in nano-porous materials under arbitrary thermomechanical loading. *J Mech Phys Solids* 2016;86:94–116. doi:10.1016/j.jmps.2015.10.005.

1 DEFENSE TECHNICAL
(PDF) INFORMATION CTR
DTIC OCA

2 DIRECTOR
(PDF) US ARMY RESEARCH LAB
RDRL CIO L
IMAL HRA MAIL & RECORDS
MGMT

1 GOVT PRINTG OFC
(PDF) A MALHOTRA

1 INST OF SHOCK PHYSICS
(PDF) IMPRL COLLEGE LONDON
L FARBANIEC

79 DIR USARL
(PDF) RDRL CIH C
E CHIN
D GROVE
J KNAP
M LEE
RDRL SE
W BENARD
RDRL WM
B FORCH
S KARNA
J LA SCALA
J MCCAULEY
A RAWLETT
S SCHOENFELD
J ZABINSKI
RDRL WML B
I BATYREV
J BRENNAN
E BYRD
S IZVYEKOV
W MATTSON
B RICE
D TAYLOR
N WEINGARTEN
RDRL WML H
B AYDELOTTE
C MEYER
D SCHEFFLER
B SCHUSTER
RDRL WMM
J BEATTY
R DOWDING
M VANLANDINGHAM
RDRL WMM B
T BOGETTI
C DECKER
C FOUNTZOULAS
G GAZONAS
D HOPKINS

B LOVE
J O'GRADY
B POWERS
T WALTER
R WILDMAN
C YEN
RDRL WMM D
J YU
A GAYNOR
B MCWILLIAMS
S WALSH
RDRL WMM E
J LASALVIA
J SWAB
D SHREIBER
RDRL WMM F
T SANO
M TSCHOPP
L KECSKES
K DARLING
RDRL WMM G
J ANDZELM
J LENHART
C RINDERSPACHER
T SIRK
Y SLIOZBERG
RDRL WMP
D LYON
RDRL WMP A
S BILYK
J CAZAMIAS
RDRL WMP B
S SATAPATHY
M SCHEIDLER
A SOKOLOV
T WEERASOORIYA
RDRL WMP C
R BECKER
T BJERKE
D CASEM
J CLAYTON
M FERREN-COKER
M GREENFIELD
B LEAVY
J LLOYD
C MEREDITH
S SEGLETES
A TONGE
C WILLIAMS
RDRL WMP D
R DONEY
C RANDOW
S SCHRAML
M ZELLNER
G VUNNI
RDRL WMP E
T JONES

INTENTIONALLY LEFT BLANK.